Active contours-driven registration method for the structure-informed segmentation of diffusion MR images☆

Oscar Esteban[a,b,*], Dominique Zosso[c], Alessandro Daducci[d], Meritxell Bach-Cuadra[e,d], María-J. Ledesma-Carbayo[a,b], Jean-Philippe Thiran[d], Andres Santos[a,b]

[a]*Biomedical Image Technologies (BIT), ETSI Telecomunicación, Universidad Politécnica de Madrid, Madrid, Spain*
[b]*Centro de Investigación Biomédica en Red en Bioingeniería, Biomateriales y Nanomedicina (CIBER-BBN), Spain*
[c]*Department of Mathematics, University of California, Los Angeles (UCLA), Los Angeles, CA, US*
[d]*Signal Processing Laboratory (LTS5), École Polytechnique Fédérale de Lausanne (EPFL), Lausanne, Switzerland*
[e]*Dept. of Radiology, CIBM, University Hospital Center (CHUV) and University of Lausanne (UNIL), Lausanne, Switzerland*

Abstract

Current applications of whole-brain tractography to diffusion MRI data require highly precise delineations of anatomical structures, which are usually projected from T1 weighted images by registration. In this study, we propose *regseg*, which is a simultaneous segmentation and registration method that uses active contours without edges extracted from structural images. The contours evolve through a free-form deformation field supported by the B-spline basis to optimally map the contours onto the data in the target space. We tested the functionality of *regseg* using four digital phantoms warped with known and randomly generated deformations, where subvoxel accuracy was achieved. We then applied *regseg* to a registration/segmentation task using 16 real diffusion MRI datasets from the Human Connectome Project, which were warped by realistic and nonlinear distortions that are typically present in these data. We computed the misregistration error of the contours estimated by *regseg* with respect to their theoretical location using the ground truth, thereby obtaining a 95% CI of 0.56–0.66 mm distance between corresponding mesh vertices, which was below the 1.25 mm isotropic resolution of the images. We also compared the performance of our proposed method with a widely used registration tool, which showed that *regseg* outperformed this method in our settings.

Keywords: active contours, cortical parcellation, diffusion MRI, nonlinear registration, segmentation, susceptibility distortion.

1. Introduction

The accurate delineation of white matter (WM) in diffusion MRI (dMRI) and the fusion of prior anatomical information extracted from a T1 weighted (T1w) image for the same subject are crucial in a range of applications based on tractography, such as the extraction of structural connectivity (Craddock et al., 2013) or tract-based spatial statistics (Smith et al., 2006). However, the precise segmentation of dMRI data and the coregistration of anatomical images are difficult due to several limitations. First, dMRI images have a resolution that is much higher than that of the imaged microstructural features (Basser and Pierpaoli, 1996). Therefore, voxels located in structural discontinuities are affected by partial voluming of the signal sources. Second, dMRI schemes probe the diffusion process within the brain at many angles to obtain diffusion weighted images (DWIs), which are completed by one or more baseline (*b0*) volumes without

☆Supplemental materials to this work will be publicly available upon publication with doi:10.6084/m9.figshare.1397502. During the review process, the document is available with the private link.

*Corresponding author
Email address: phd@oscaresteban.es (Oscar Esteban)

directional gradients. The extremely low signal-to-noise ratio (SNR) and the high dimensionality of DWIs prevent their direct use in segmentation. The low contrast between grey matter (GM) and WM in the *b0* volumes also makes them unsuitable for segmentation. Finally, dMRI images are acquired using echo-planar imaging (EPI) to speed up the acquisition process but at the cost of introducing geometrical distortion, as well as signal degradation and destruction (Jezzard and Balaban, 1995). The artifacts generated have major impacts on the anatomy extracted from dMRI, particularly in certain fiber bundles (Irfanoglu et al., 2012). These limitations prevent segmentation in the native dMRI space, including registration-based approaches using anatomical images as the sources of structural information.

Early attempts to delineate the WM involved thresholding the fractional anisotropy (FA)[1] map. However, the mask and subsequent analyses are highly dependent on the threshold set (Taoka et al., 2009). To overcome the unreliability of FA thresholding, Zhukov et al. (2003) proposed active contours with edges represented by level sets, which evolve on directionally invariant scalar maps. Rousson et al. (2004) successfully segmented the corpus callosum with region-based level sets based on the eigenvalues of tensors fitted using the dMRI data. Many studies have addressed the definition of appropriate features for clustering, such as the 5D representation proposed by Jonasson (2005). Other efforts include mixed models based on sets of directionally invariant maps (Liu et al., 2007), iterative (Hadjiprocopis et al., 2005) and hierarchical (Lu et al., 2008) clustering, graph-cuts (Han et al., 2009), and volume fraction modeling (Kumazawa et al., 2013).

To address the segmentation problem by registration, Saad et al. (2009) used the Pearson's correlation coefficient to obtain a linear alignment of the T1w and the *b0*. Similarly, a linear registration method was employed by *bbregister* (Greve and Fischl, 2009), which uses active contours with edges to search for intensity boundaries in the *b0* image. The active contours are initialized using surfaces extracted from the T1w using *FreeSurfer* (Fischl, 2012): the *pial* surface (exterior of the cortical GM) and the *white* surface (the WM/GM interface). The *b0* image only includes a detectable frontier for the pial surface, so *bbregister* is limited to aligning the cortical layer in this application. This tool has become the standard method because of its proven robustness, although the distortions found in dMRI are nonlinear. To overcome this issue, *bbregister* excludes the regions that are typically warped by artifacts from the boundary search. However, because the distortion is not considered, it must be addressed separately. Nonlinear registration has been performed successfully between T2 weighted (T2w) and *b0* images based on their similarity as a unique method for correcting distortion (Kybic et al., 2000; Studholme et al., 2000; Wu et al., 2008; Tao et al., 2009). However, further registration of the T1w and T2w images is still required to map the anatomical information (and for WM segmentation) into the dMRI space.

Therefore, given these issues, a method that simultaneously performs segmentation in the native dMRI space and registration of the corresponding T1w image onto the dMRI data could provide the optimal solution. To the best of our knowledge, this strategy has never been proposed for the application described above. Previously, joint segmentation and registration have been applied successfully to other problems such as longitudinal object tracking (Paragios, 2003) and atlas-based segmentation (Gorthi et al., 2011). The most thorough approach integrates active contours during image registration methods. Unal and Slabaugh (2005), and later Wang et al. (2006), improved an existing method (Yezzi et al., 2003) based on linear registration to the nonlinear case by implementing a free-form deformation field. Droske et al. (2009) reviewed the existing techniques and proposed two different approaches for applying the Mumford-Shah functional (Mumford and Shah, 1989) during simultaneous registration and segmentation by propagating the deformation field from the contours onto the whole image definition. Recently, Le Guyader and Vese (2011) proposed a simultaneous segmentation and registration method in 2D using level sets and a nonlinear elasticity smoother on the displacement vector field, which preserves the topology even with very high deformation. Finally, Gorthi et al. (2011) extended the existing methodologies using a multiphase level set function to register several active contours during the application of atlas-based segmentation.

The hypothesis tested in the present study is that registration and segmentation problems in dMRI can be solved simultaneously, thereby increasing the geometrical accuracy of the process. Thus, we propose

[1] the FA is a scalar parameter of diffusion derived from the dMRI data.

a tool called *regseg* that exploits the prior information of shapes extracted using T1w images to register the anatomical reference to dMRI space, thereby implicitly segmenting these data. The proposed approach uses active contours without edges (Chan and Vese, 2001), which evolve to drive a free-form deformation field of B-spline basis functions. Optimization is performed using a descent strategy with explicit shape gradients (Jehan-Besson et al., 2003; Herbulot et al., 2006). Therefore, unlike most previous methods, *regseg* does not implement level sets. The nonlinear distortion is aligned with one of the imaging axes (see subsection 2.5), so *regseg* includes an anisotropic regularizer for the displacements field proposed by Nagel and Enkelmann (1986). Finally, we evaluated *regseg* using an extension of our instrumentation framework (Esteban et al., 2014), which simulates known and realistic distortions based on dMRI data. The evaluation included a comparison with T2w-registration based (T2B) correction by integrating it within the framework of an in-house implementation of the method.

2. Methods

Let $\mathbf{\Gamma}_R = \{\Gamma_m : m \in \mathbb{N}, m \leq N_S\}$ be the set of N_S surfaces extracted from the undistorted T1w image (the reference space R). We reformulate the segmentation of the distorted dMRI images (the moving space M) as a registration problem where we search for an underlying deformation field U such that the structures in R defined by $\mathbf{\Gamma}_R$ align optimally with their corresponding structures in M:

$$\begin{aligned} U\colon R \subset \mathbb{R}^n &\to M \subset \mathbb{R}^n \\ \mathbf{r} &\mapsto \mathbf{r}' = \mathbf{r} + \mathbf{u}(\mathbf{r}), \end{aligned} \tag{1}$$

where $\mathbf{r}$ denotes a position in R, $\mathbf{r}'$ is its corresponding location in M, and n denotes the dimensionality of images. Finally, $\mathbf{u} = \mathbf{u}(\mathbf{r})$ is the displacement of every point with respect to the reference domain.

2.1. Cost-function derivation

In a Bayesian framework for registration (Wyatt and Noble, 2003; Pohl et al., 2006; Gass et al., 2014), the mappings U in (1) are evaluated based on their posterior probability given the observed data M. Let $\mathbf{\Omega} = \{\Omega_l : l \in \mathbb{N}, l \leq N_L\}$ be the set of N_L competing regions in which M is partitioned by the projection of $\mathbf{\Gamma}_R$. Using Bayes' rule, the posterior likelihood is computed as:

$$P(U \mid M, \mathbf{\Omega}) = \frac{P(M \mid U, \mathbf{\Omega})\, P(U)}{P(M)}, \tag{2}$$

where $P(M \mid U, \mathbf{\Omega})$ is the data likelihood. Because $\mathbf{\Omega}$ are mapped by U, then we simplify $P(U, \mathbf{\Omega}) = P(U) \implies P(M \mid U, \mathbf{\Omega}) = P(M \mid U)$. The best estimate $\hat{U}$ then satisfies the maximum a posteriori criterion (Bishop, 2006) and it aligns $\mathbf{\Gamma}_R$ into M. First, we assume independence between pixels, and thus we break down the global data likelihood into a product of pixel-wise conditional probabilities:

$$P(M \mid U) = \prod_l \prod_{\mathbf{r} \in \Omega_l} P\left(\mathbf{f}' \mid U\right), \tag{3}$$

where $\mathbf{f}' = M(\mathbf{r}')$ is the feature vector at the displaced position $\mathbf{r}'$ (1) in the moving image. For convenience and because it has been shown to be an appropriate approximation (Van Leemput et al., 1999; Cuadra et al., 2005), we introduce two assumptions for each region Ω_l: 1) the features are i.i.d.; and 2) they can be modeled by multivariate normal distributions with the parameters $\{\boldsymbol{\mu}_l, \mathbf{\Sigma}_l\}$ for each region Ω_l:

$$P(M \mid U) = \prod_l \prod_{\mathbf{r} \in \Omega_l} \mathcal{N}(\mathbf{f} \mid \boldsymbol{\mu}_l, \mathbf{\Sigma}_l) = \prod_l \prod_{\mathbf{r} \in \Omega_l} \frac{1}{\sqrt{(2\pi)^C \ |\mathbf{\Sigma}_l|}}\, e^{\left(-\frac{1}{2}\mathcal{D}_l^2(\mathbf{f}')\right)}, \tag{4}$$

using $\mathcal{D}_l^2(\mathbf{f})$ to denote the squared *Mahalanobis distance* of $\mathbf{f}$ with respect to the descriptors of region l as $\mathcal{D}_l^2(\mathbf{f}) = (\mathbf{f} - \boldsymbol{\mu}_l)^T \boldsymbol{\Sigma}_l{}^{-1} (\mathbf{f} - \boldsymbol{\mu}_l)$. C is the number of channels comprised in the image M. In fact, the projection of $\boldsymbol{\Gamma}_R$ onto M is an implicit segmentation model, for which the covariance matrix $\boldsymbol{\Sigma}_l$ of each region is minimized.

The smoothness of the resulting displacements field is induced by a Thikonov regularization prior:

$$P(U) = \prod_{\mathbf{r}} p(\mathbf{u}) = \prod_{\mathbf{r}} p_0(\mathbf{u})\, p_1(\mathbf{u}), \text{ with} \tag{5}$$

$$\begin{aligned} p_0(\mathbf{u}) &= \mathcal{N}(\mathbf{u} \mid 0, \mathbf{A}^{-1}), \\ p_1(\mathbf{u}) &= \mathcal{N}(\nabla\mathbf{u} \mid 0, \mathbf{B}^{-1}), \end{aligned} \tag{6}$$

which requires that the distortion and its gradient have zero mean and variance governed by the matrices $\mathbf{A}$ and $\mathbf{B}$. Finally, the maximum a posteriori problem is adapted to a variational problem where we search for the minimum of an energy functional by applying $E(\mathbf{u}) = -\log\{P(M \mid U)\, P(U)\}$:

$$\begin{aligned} E(\mathbf{u}) &= -\log \prod_l \prod_{\mathbf{r}\in\Omega_l} \mathcal{N}\left(\mathbf{f}' \mid \boldsymbol{\mu}_l, \boldsymbol{\Sigma}_l\right)\, p_0(\mathbf{u})\, p_1(\mathbf{u}) = \\ &= \text{Const.} + \sum_l \int_{\Omega_l} \mathcal{D}_l^2(\mathbf{f}')\, d\mathbf{r} \; + \int_\Omega \frac{1}{2}\left[\mathbf{u}^T\mathbf{A}\mathbf{u} + (\nabla\mathbf{u})^T\mathbf{B}(\nabla\mathbf{u})\right]\, d\mathbf{r}. \end{aligned} \tag{7}$$

This expression is the dual of the Mumford-Shah functional that corresponds to the framework of active contours without edges (Chan and Vese, 2001) with the anisotropic regularization term of Nagel and Enkelmann (1986).

2.2. Numerical Implementation

Deformation model. Since the vertices of the surfaces $\{\mathbf{v}_i : \mathbf{v}_i \subset \boldsymbol{\Gamma}\}_{i=1\ldots N_V}$ are probably located off-grid, it is necessary to derive $\mathbf{u}_i = \mathbf{u}(\mathbf{v}_i)$ from a discrete set of parameters $\{\mathbf{u}_k\}_{k=1\ldots K}$. Densification is achieved using a set of associated basis functions ψ_k (8). In our implementation, ψ_k is selected as a tensor-product B-spline kernel of degree three.

$$\mathbf{v}_i' = \mathbf{v}_i + \mathbf{u}_i = \mathbf{v}_i + \sum_k \psi_k(\mathbf{r})\, \mathbf{u}_k. \tag{8}$$

Optimization. To find the minimum of the energy functional (7), we propose a gradient-descent approach with respect to the underlying deformation field using the following partial differential equation (PDE):

$$\frac{\partial \mathbf{u}(\mathbf{r}, t)}{\partial t} \propto -\frac{\partial E(\mathbf{u})}{\partial \mathbf{u}_k}, \tag{9}$$

where t is an artificial time parameter of the contour evolution and $\mathbf{u}_k$ are the parameters that support the estimate $\hat{U}$ of the transformation at the current time point. Let us assume that the anisotropy is aligned with the imaging axes to simplify (7) as expression (A.1) in Appendix 1, and thus to compute its derivative (9):

$$\frac{\partial E(\mathbf{u})}{\partial \mathbf{u}_k} = \frac{\partial}{\partial \mathbf{u}_k}\Big\{\sum_l \int_{\Omega_l} \mathcal{D}_l^2(\mathbf{f}')\, d\mathbf{r} \; + \int_\Omega \frac{1}{2}[\boldsymbol{\alpha}\cdot\mathbf{u}^{\circ 2} + \boldsymbol{\beta}\cdot(\nabla\mathbf{u})^{\circ 2}]\, d\mathbf{r}\Big\}, \tag{10}$$

where $\mathbf{u}^{\circ 2} = \mathbf{u}^T \cdot \mathbf{u}$. Then, the data and regularization terms are split and discretized to compute their derivatives. The computation of the explicit shape gradients at each $\mathbf{v}_i'$ is illustrated in Figure 1. Then, (10) can be reformulated as (see Supplemental Materials, equations SM6-SM12):

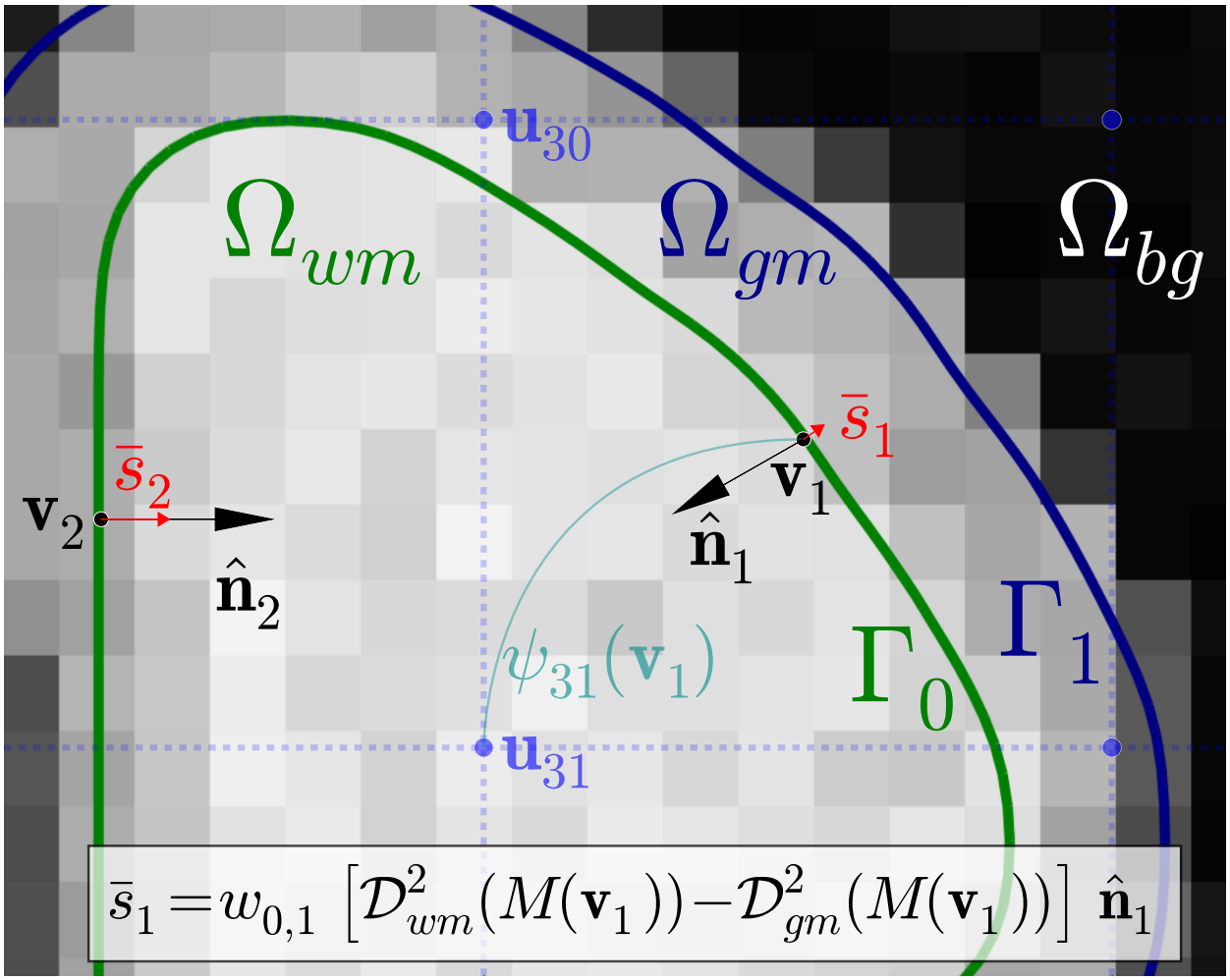

Figure 1: The active contours are defined as the interfacing surfaces of the competing ROIs Ω_i, which are represented in green and dark blue in this close-up. They evolve iteratively following their inward normals $\hat{n}_i$ at each vertex $\mathbf{v}_i$ of the mesh. The gradient speeds $\bar{s}_i$ drive registration, which are computed as the disparity of the data energies with respect to the two limiting regions of $M(\mathbf{v}_i)$, the features of the image M in the location of vertex $\mathbf{v}_i$ (see Supplemental Materials, equation SM5). In this figure, $\bar{s}_1$ is written in the lower box, with Ω_{wm} in the inner limiting region, Ω_{gm} the outer region, and $w_{0,1}$ is the relative area associated with vertex $\mathbf{v}_1$ with respect to the total area of surface Γ_0.

$$\frac{\partial E(\mathbf{u})}{\partial \mathbf{u}_k} = \mathbf{g}_k + \boldsymbol{\alpha} \cdot \mathbf{u}_k - \boldsymbol{\beta} \cdot (\Delta \mathbf{u}_k). \tag{11}$$

Finally, to descend this gradient, we establish a semi-implicit Euler scheme (see Supplemental Materials, section S1.3), with a step size parameter δ, which we solve in the spectral domain as follows:

$$\mathbf{u}_k^{t+1} = \mathcal{F}^{-1}\left\{\frac{\mathcal{F}\{\delta^{-1}\,\mathbf{u}_k^t - \mathbf{g}_k\}}{\mathcal{F}\{(\delta^{-1} + \boldsymbol{\alpha})\,I - \boldsymbol{\beta}\Delta\}}\right\}, \tag{12}$$

where I denotes the identity operator.

Implementation details, settings, and convergence. The *regseg* tool includes a multiresolution strategy on the free-form deformation field. Registration pyramids are created by setting the spacing between the control points of the B-spline basis functions for each level of the multiresolution strategy. The implementation details as well as other features (such as the sparse matrix approach to fast interpolation) and the main parameters (such as δ, $\boldsymbol{\alpha}$, $\boldsymbol{\beta}$, the B-spline grid resolutions, and target image smoothing) are discussed in Supplemental Materials, section S1. The actual choices of the parameter settings are publicly distributed with the source code for the experiments. The final settings were obtained manually based on feedback from the post-registration convergence reports (such as that found in Supplemental Materials, section S1.3). We released *regseg* along with the tool to generate the convergence report.

2.3. Evaluation protocol

In order to assess the performance of *regseg*, we defined the following general evaluation protocol: 1) Extract the set of undistorted surfaces $\boldsymbol{\Gamma}_R$; 2) Compute a ground-truth field of displacements U_{true}, which is applied to generate warped images (M) for segmentation; 3) Execute *regseg* with $\boldsymbol{\Gamma}_R$ and use the warped data as inputs; and 4) Perform a visual assessment and compute the error metrics. The adaptation of this protocol to the simulated phantoms and real data is explained in the following sections.

2.4. Simulated phantoms

The workflow required to simulate the digital phantoms and to assess the performance of *regseg* with them is presented in Figure 2. A set of four binary objects (i.e., "box", "ball", "L", and "gyrus") was generated by combining the binarization of analytical shapes and mathematical morphology. The reference surfaces $\boldsymbol{\Gamma}_R$ were extracted from the binary shapes using *FreeSurfer* tools (Fischl, 2012). The ground-truth distortion was generated using a chain of two displacement fields supported by grids of B-spline basis functions. The coefficients of the basis functions were generated randomly for both levels in their three dimensions. The three components of the displacements $\mathbf{u} = (u_d)$ were bounded above by 40% of the separation between the control points at each level to obtain diffeomorphic transforms after concatenation (Rueckert et al., 2006). The first deformation field was applied to generate large warpings with control points separated by 50.50 mm in the three dimensions ($u_d \leq 20.20$ mm). With the second warping, we aimed to obtain a field with smoothness close to that found in a typical distortion field of dMRI data (Irfanoglu et al., 2011). Therefore, the control points were separated by 25.25 mm ($u_d \leq 10.10$ mm). After generating the ground-truth deformation, the original surfaces were warped by interpolating the displacements field at each vertex. The warped surfaces $\boldsymbol{\Gamma}_{\text{true}}$ were binarized to generate tissue fractions at low (2.0×2.0×2.0 [mm]) and high (1.0×1.0×1.0 [mm]) resolutions. Using a magnetic resonance (MR) simulator (Caruyer et al., 2014), we synthesized T1w (TE/TR= 10/1500 ms) and T2w images (TE/TR= 90/5000 ms), which corresponded to each phantom type, with each at two resolutions (1.0 mm and 2.0 mm isotropic). The field of view at both resolutions was 100×100×100 [mm]. Next, *regseg* was applied to map $\boldsymbol{\Gamma}_R$ onto the warped phantoms to obtain the registered surfaces ($\hat{\boldsymbol{\Gamma}}_{test}$). To quantify the misregistration error, we computed the Hausdorff distance between $\hat{\boldsymbol{\Gamma}}_{test}$ and $\boldsymbol{\Gamma}_{\text{true}}$ using (Commandeur et al., 2011).

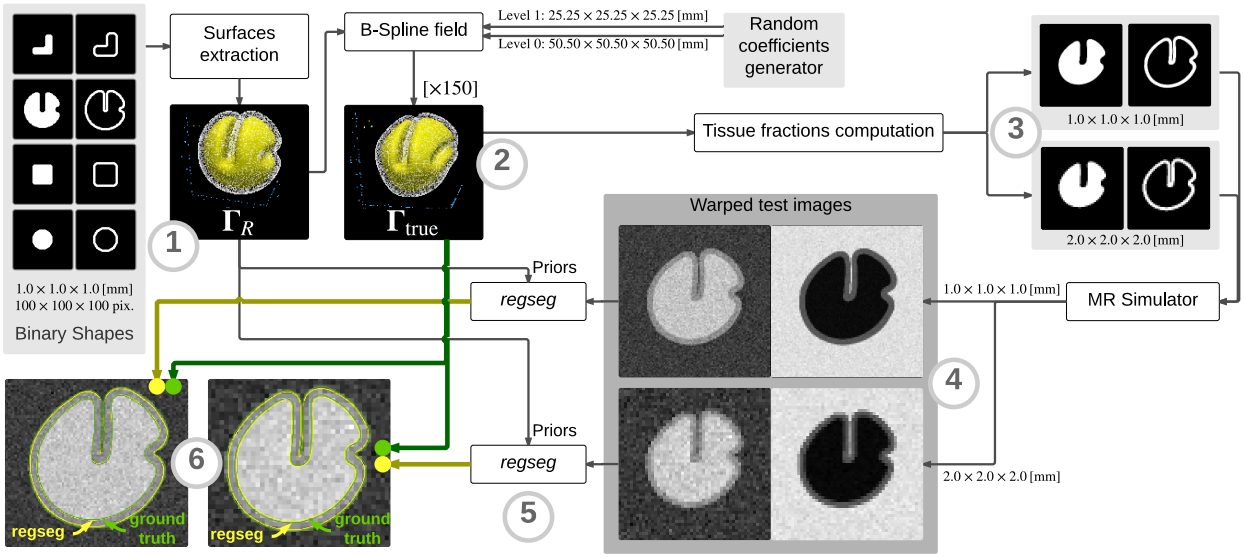

Figure 2: Evaluation of *regseg* using phantom data according to the following instrumental workflow. 1) The reference surfaces $\mathbf{\Gamma}_R$ are triangularized meshes extracted from the four binary shapes (i.e., "box", "ball", "L", "gyrus"). 2) A ground-truth displacement field was generated as described in subsection 2.4, and applied to warp $\mathbf{\Gamma}_R$, thereby obtaining $\mathbf{\Gamma}_{\text{true}}$. 3) After being warped, $\mathbf{\Gamma}_{\text{true}}$ were projected onto the corresponding discrete 3D volume and downsampled to create partial volume effects at two resolutions, i.e., 2.0×2.0×2.0 [mm] and 1.0×1.0×1.0 [mm], thereby producing sets of tissue fractions maps. 4) The tissue fractions were fed into a magnetic resonance (MR) simulator, which generated T1 weighted (T1w) and T2 weighted (T2w) -like images at the two possible resolutions. 5) The *regseg* tool was applied using the warped test images as multispectral moving images and $\mathbf{\Gamma}_R$ as shape priors. 6) The agreement between the surfaces fitted by *regseg* ($\hat{\mathbf{\Gamma}}_{test}$) and $\mathbf{\Gamma}_{\text{true}}$ were assessed visually using automatically generated visual reports and quantitatively with the Hausdorff distance between the corresponding surfaces.

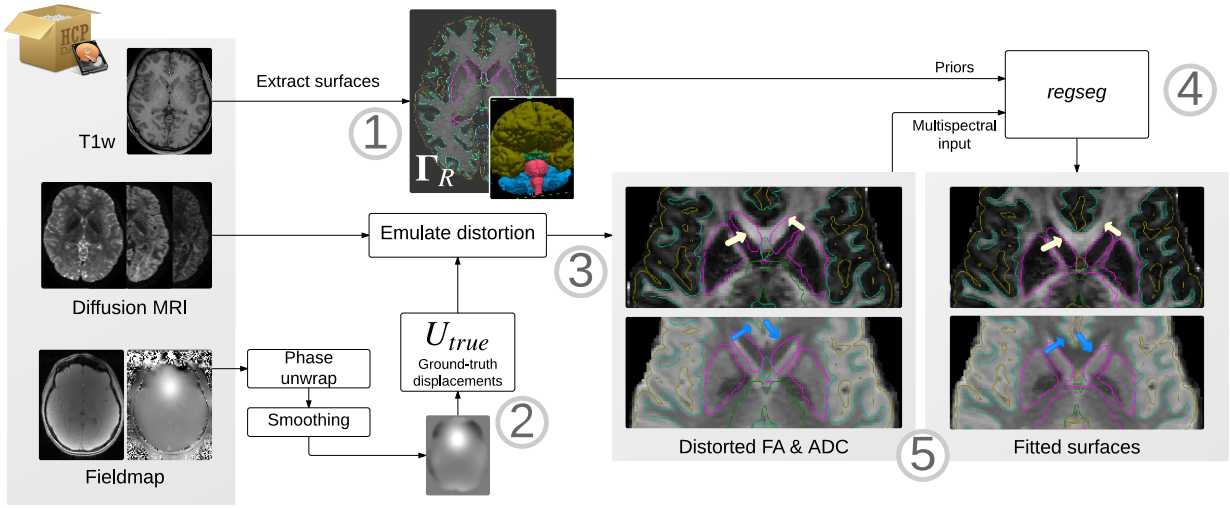

Figure 3: Experimental workflow employed to process real data from the Human Connectome Project (HCP). 1) $\mathbf{\Gamma}_R$ were extracted from the anatomical reference (T1w image). 2) For use as the ground truth, we generated a plausible synthetic distortion U_{true} from the field map with (13). 3) The dMRI data were warped using U_{true} to reproduce the effects of real susceptibility-derived distortions. Target diffusion scalars (FA and ADC) were computed with the distorted data and stacked to feed the multivariate input required by *regseg*. 4) The method was run to obtain $U_{test} = \hat{U}_{true}$, i.e., the estimate of the ground-truth deformation. 5) The results were evaluated visually and quantitatively.

2.5. Real datasets

The general experimental framework for the real datasets is presented in Figure 3, which extends our previous evaluation (Esteban et al., 2014) of distortions using dMRI phantoms.

Data. To evaluate *regseg* using real dMRI data obtained from human brains, we collected 16 subjects from the Human Connectome Project (HCP) database. The original acquisitions are released within "unprocessed" packages, whereas the "minimally preprocessed" packages contain the corresponding images after some processing (correction for several artifacts, brain-extraction, spatial normalization, etc.). We refer the reader to (Van Essen et al., 2012) for exact details of the acquisition parameters and (Glasser et al., 2013) for the preprocessing issues. These datasets comprise a large set of images, including T1w, T2w, and multi-shell dMRI images.

Segmentation model. Based on our experience and previous studies (Ennis and Kindlmann, 2006), we defined the moving image as a stack of the FA and ADC maps derived from dMRI data. After evaluating several alternative models, we empirically defined a partition $\mathbf{\Omega}$ according to the following six regions: 1) thalamus (Ω_{Tha}); 2) ventricular system and deep GM structures (Ω_{VdGM}); 3) cerebral WM (Ω_{WM}); 4) brain stem and cerebellar WM (Ω_{bst}); 5) cerebellar GM (Ω_{cbGM}); and 6) cortical GM (Ω_{GM}). Using tools in *FreeSurfer* and appropriate selections of labels in the *aparc* segmentation released with the HCP data, we extracted the $\mathbf{\Gamma}_R$ set for the reference surfaces. The segmentation model corresponding to this partition is shown in Figure 4 and discussed in greater detail in Supplemental Materials, section S4.

Ground-truth generation. Realistic deformation is achieved by generating displacements fields that satisfy the theoretical properties of distortion (Jezzard and Balaban, 1995). The displacements along the phase-encoding (PE) axis of the dMRI image are related to the local deviation of the field $\Delta B_0(\mathbf{r})$ from its nominal value B_0, as follows:

$$u_{\text{PE}} = \frac{\gamma\, T_{acq}\, s_{\text{PE}}}{2\pi} \Delta B_0(\mathbf{r}) \text{ [mm]}, \tag{13}$$

where γ is the gyromagnetic ratio, T_{acq} is the readout time, and s_{PE} is the pixel size along PE. Certain MR sequences are designed to estimate ΔB_0, thereby obtaining the so-called field map. We derived the deformation U_{true} from the field map image released with the corresponding packages of each dataset in the HCP. The field map was unwrapped[2] and smoothed before applying (13). Next, the original dMRI was warped using the resulting displacement field and fed into a pipeline to process the corresponding diffusion tensor image (DTI), thereby computing the derived scalars of interest (FA and ADC) using *MRtrix* (Tournier et al., 2012).

Metric assessment. Initially, we investigated the appropriateness of the segmentation model. For five test datasets, we uniformly sampled the space of distortions $\hat{U} = \epsilon \cdot U_{true} = \mathbf{r} + \epsilon\, u_{\text{PE}}$ (with $\epsilon \in [-1.1, 1.1]$ and u_{PE} from (13)), and we evaluated the data term of the cost function (7). The minimum of the cost function (subsection 2.1) was consistently located at $\epsilon = 0.0$ (the ground-truth) for all of the cases (Supplemental Materials, Figure S2).

Cross-comparison. A similar workflow to the general evaluation framework used for Figure 3 was employed to integrate the alternate T2B registration scheme. We reproduced the solution and settings provided with *ExploreDTI* (Leemans et al., 2009), which is a widely used toolkit for tractography analysis of DTI. *ExploreDTI* internally employs *elastix* (Klein et al., 2010) to perform registration.

[2] fieldmaps are phase maps, which are intrinsically clipped in the interval of $[-\pi, \pi)$ [rads] or [rads/s].

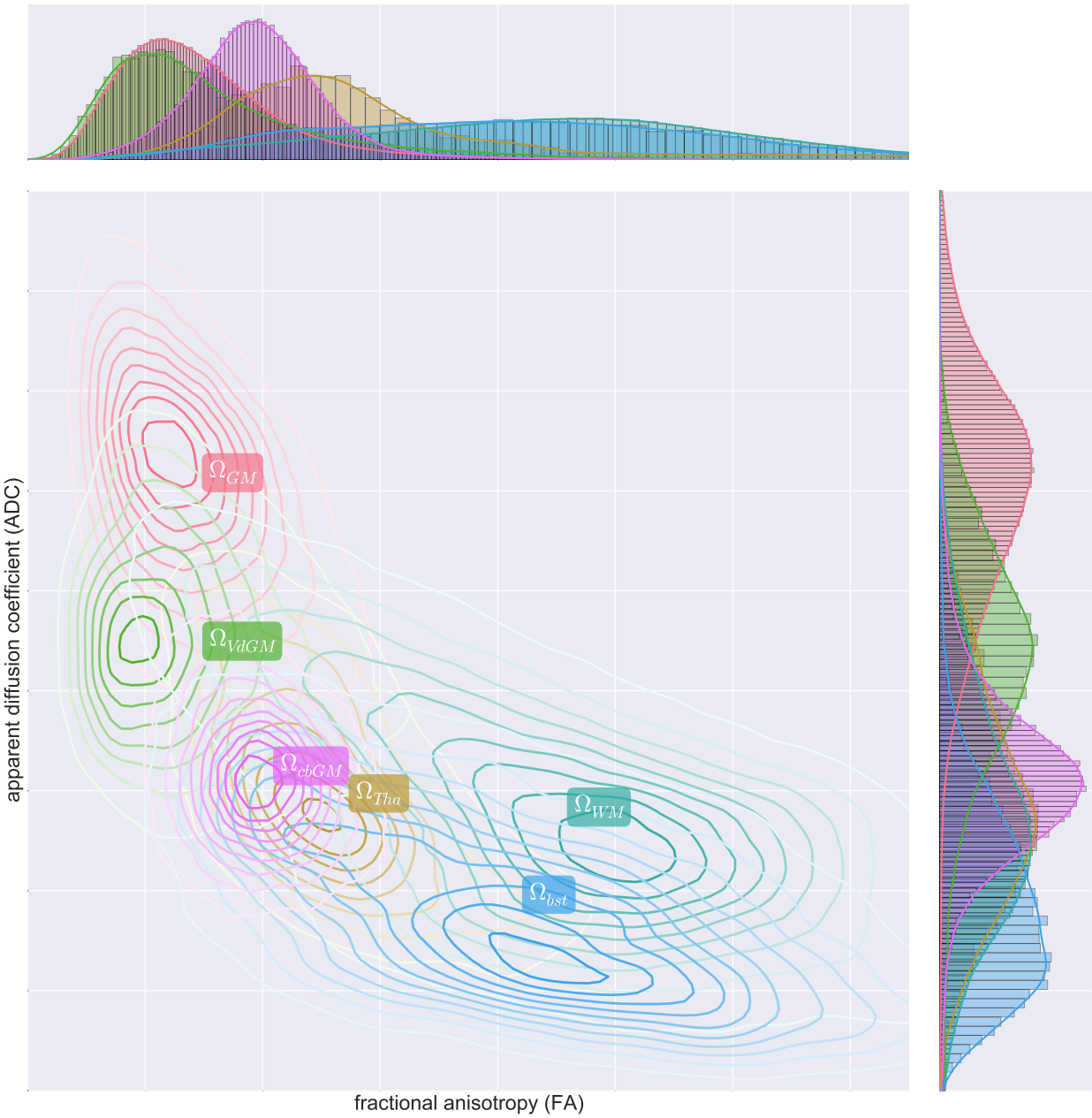

Figure 4: Segmentation model defined by the homogeneous regions Ω_i, where the image for segmentation is partitioned by the theoretical projection ($\mathbf{\Gamma}_{true}$) of $\mathbf{\Gamma}_R$ onto M. The plot represents a kernel density estimate of the location and spread of each region Ω_i in the bivariate feature space of M, which comprises the FA and ADC maps. At the top and the right margins, the marginal distributions of Ω_i are also plotted for the FA and ADC, respectively.

Res.	"gyrus"	"ball"	"box"	"L"	Aggreg.
1.0mm	0.18-0.38	0.31-0.45	0.34-0.42	0.34-0.40	0.34-0.38
2.0mm	0.59-0.60	0.65-0.76	0.68-0.71	0.67-0.77	0.64-0.66

Table 1: The distributions of vertex-wise Hausdorff distances between the ground-truth surfaces and their corresponding estimates obtained with *regseg* presented a 95% CI below the half-voxel size for all of the phantom types. The CIs were computed by bootstrapping using 10^4 samples, with the median as the location statistic.

Error measurement. Distortion only occurs along the PE axis of the image, so we computed the surface warping index (sWI) as the area-weighted distance between the corresponding vertices of $\mathbf{\Gamma}_{true}$ and their estimate obtained by the method under the test $\hat{\mathbf{\Gamma}}_{test}$:

$$sWI = \frac{1}{\sum_i a_i} \sum_i^{N_V} a_i \left\| \mathbf{v}_i - \hat{\mathbf{v}}_i \right\|, \tag{14}$$

where $\mathbf{v}_i \subset \mathbf{\Gamma}_{\text{true}}$ are the locations of the total N_V vertices and $\hat{\mathbf{v}}_i \subset \hat{\mathbf{\Gamma}}_{test}$ are the recovered locations that correspond to $\mathbf{v}_i$. In practice, we only report the sWI for three surfaces of crucial interest in whole-brain tractography. These three surfaces delineated the following regions in the model: Ω_{VdGM}, Ω_{WM}, and Ω_{GM}.

3. Results

3.1. Proof of concept using digital phantoms

In total, 1200 experiments (four phantom types $\times$ 150 random warpings $\times$ two resolutions) were performed according to the workflow illustrated in Figure 2. For each experiment, the misregistration error was measured using the Hausdorff distance (see section 2.5) between the theoretical $\mathbf{\Gamma}_{\text{true}}$ and the estimate obtained by *regseg* ($\hat{\mathbf{\Gamma}}_{test}$). The results demonstrated that the accuracy was consistent and high, and below the image resolution. Figure 5 (block C) shows the violin plots for each model type corresponding to the two sets of resolutions for the generated phantoms. In order to relate the average misregistration error to the resolution of the moving image, we proceeded as follows. First, we confirmed that the vertex-wise error distributions were skewed by using Shapiro-Wilk's test of normality. All of the distributions of errors in the tests (four phantom types $\times$ two resolutions) were non-normal with $p < 0.001$. Consequently, we used the non-parametric Wilcoxon signed-rank test with the Bonferroni correction for multiple comparisons ($N = 150$, for each phantom type). The average errors were significantly lower than the voxel size with $p < (0.001/150)$ in all tests (four phantom types $\times$ two resolutions). Statistical tests might not be sufficiently conclusive, so we also computed the confidence intervals, as shown in Table 1.

3.2. Evaluation using real datasets and cross-comparison

Finally, we compared the performance of *regseg* with that of the standard T2B method. Summary reports for visual assessment of the 16 cases are included in Supplemental Materials, section S5. In Figure 6, box A, the visual report is shown for one subject. We computed the sWI (14) of every surface after registration using both the *regseg* and T2B methods. Finally, to compare the results, we performed Kruskal-Wallis H-tests (a non-parametric alternative to ANOVA) on the warping indices for the three surfaces of interest selected in section 2.5 (Γ_{VdGM}, Γ_{WM}, Γ_{pial}). All of the statistical tests showed that the error distributions obtained with *regseg* and T2B were significantly different, and the violin plots in box B of Figure 6 demonstrate that the errors were always larger with T2B. We also show the 95% CIs of the sWI for these surfaces. The aggregate CI for *regseg* was 0.56–0.66 [mm], whereas the T2B method yielded an aggregate CI of 2.05–2.39 [mm]. The results of the statistical tests and the CIs are summarized in Table 2.

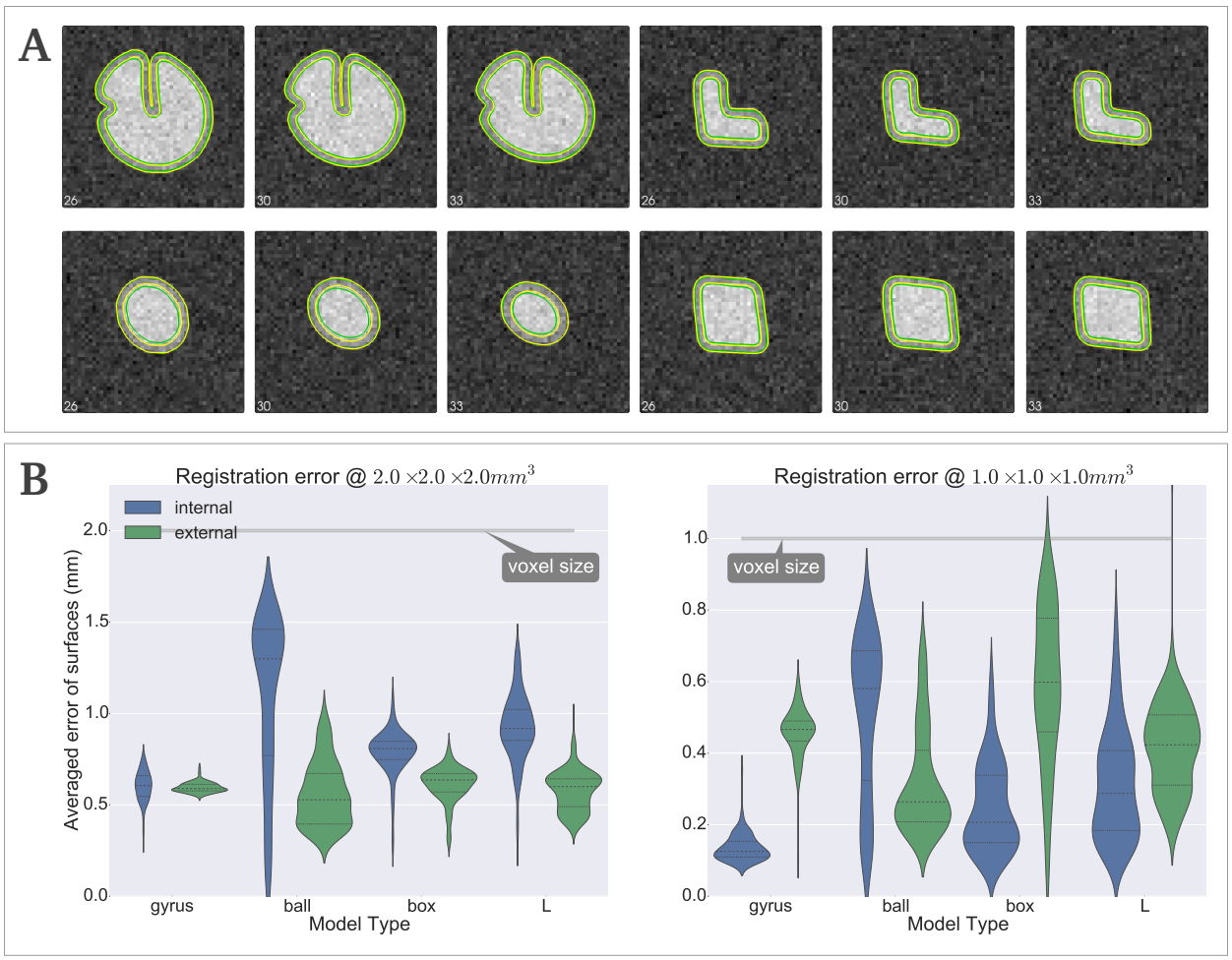

Figure 5: A. Visual assessment of the results obtained with the low resolution sets: "gyrus" (top left), "L" (top right), "ball" (bottom left), and "box" at (bottom right). The contours recovered after registration are represented in yellow. *Regseg* achieved high accuracy because it determined the almost exact locations of the registered contours with respect to their ground truth positions (shown in green). The partial volume effect makes segmentation of the sulci a challenging problem with voxel-wise clustering methods, but they were successfully segmented with *regseg*. B. Quantitative evaluation of registration errors in terms of the average Hausdorff distances between surfaces at low (left) and high (right) resolutions, which demonstrate that the errors were consistently below the size of the voxels.

		Γ_{VdGM}	Γ_{WM}	Γ_{pial}	Aggreg.
CI	*regseg*	0.50 - 0.78	0.50 - 0.55	0.66 - 0.73	0.56 - 0.66
	T2B	1.78 - 2.58	1.94 - 2.36	2.16 - 2.58	2.05 - 2.39
H-tests	p-value	4.1×10^{-6}	2.3×10^{-6}	2.3×10^{-6}	1.8×10^{-16}
	H-stat	21.20	22.31	22.31	67.85

Table 2: Statistical analysis of results obtained using real data, which show that *regseg* performed better than the alternative T2w-registration based (T2B) method. The distribution of the errors computed for the surfaces of interest (Γ_{VdGM}, Γ_{WM}, Γ_{pial}) and the aggregate of all surfaces (Aggreg. column) had lower 95% CIs with *regseg*. The CIs in this table were computed by bootstrapping using the mean as the location statistic and with 10^4 samples. The Kruskal-Wallis H-tests indicated that there was a significant difference between the results obtained using *regseg* and the T2B method.

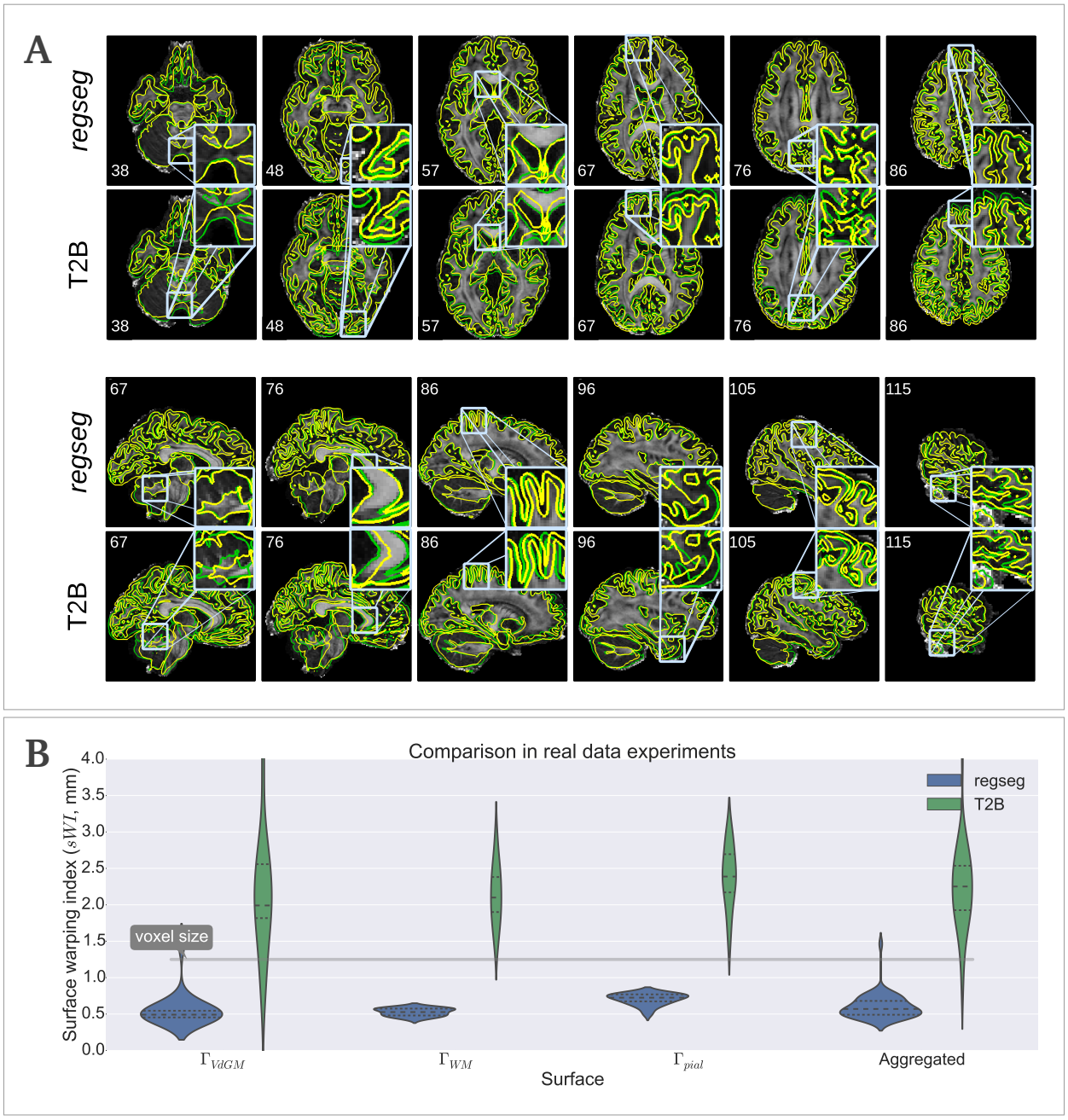

Figure 6: A. Example of a visual assessment report, which was generated automatically by the evaluation tool. Each view shows one component of the input image (in this case, the FA map), the ground-truth locations of the surfaces (green contours), and the resulting surfaces obtained with the test method (yellow contours). The first two rows show axial slices for *regseg* and the T2w-registration based (T2B) method, while the last two rows show the corresponding sagittal views. The coronal view is omitted because it was the least informative due to the directional property of the distortions. Specific regions where *regseg* outperformed T2B are enlarged. B. Violin plots of the error distributions for each surface, which show the voxel size of the dMRI images (1.25 mm), thereby supporting the improved results obtained by *regseg* with the proposed settings.

4. Discussion

Accuracy tests. The hypothesis tested in our study was that reliable image registration can be performed by searching for homogeneous regions in a multispectral image, which correspond to precise contours from an atlas, or extracted from another image (i.e., a different time step). We demonstrated that active contours without edges can be used successfully to drive a deformation supported by B-spline basis functions with digital phantoms. We randomly deformed four different phantom models to mimic three homogeneous regions (WM, GM, and cerebrospinal fluid) and we used them to simulate T1w and T2w images at two resolution levels. After registration with *regseg*, we measured the Hausdorff distance between the projected contours obtained using the ground-truth warping and our estimates. We concluded that the errors were significantly lower than the voxel resolution. We also assessed the 95% confidence interval (CI), which yielded an aggregate interval of 0.64–0.66 [mm] for the low resolution phantoms (2.0 mm isotropic voxel) and 0.34–0.38 [mm] for the high resolution phantoms (1.0 mm isotropic). Therefore, we also concluded that the error was bounded above by half of the voxel spacing.

Application to real data. We designed *regseg* as a method for segmenting dMRI data by exploiting the anatomical information extracted from the corresponding T1w image of the subject. Applications in whole-brain tractography (Smith et al., 2006; Craddock et al., 2013) usually solve this problem with a two-step approach. First, the images are corrected for nonlinear distortions using auxiliary acquisitions such as field maps (Jezzard and Balaban, 1995), T2w images (Kybic et al., 2000). Second, the segmentation is projected from a reference T1w image using linear registration (Greve and Fischl, 2009). *Regseg* addresses this joint problem in a single step and it does not require any additional acquisition other than the minimal protocol using only T1w and dMRI images. This situation is found commonly in historical datasets.

We evaluated *regseg* in a real environment using the experimental framework presented in Figure 3. We processed 16 subjects from the HCP database using both *regseg* and an in-house replication of the T2w-registration based (T2B) method. *Regseg* obtained very high accuracy, with an aggregate 95% CI of 0.56–0.66 [mm], which was below the pixel size of 1.25 mm. The misregistration error that remained after *regseg* was significantly lower ($p < 0.01$) than the error corresponding to the T2B correction according to Kruskal-Wallis H-tests (Table 2). Visual inspections of all the results (Supplemental Materials, section S5) and the violin plots in Figure 6 confirmed that *regseg* performed better than the T2B method in our settings. We carefully configured the T2B method using the same algorithm and the same settings employed in a widely-used tool. However, cross-comparison experiments are prone to so-called *instrumentation bias* (Tustison et al., 2013). Therefore, these results do not prove that *regseg is better than* T2B. Our results suggest that *regseg* is a reliable option in this application field. In addition, the T2B may introduce an additional (and small) error during the necessary registration of T2w in the T1w space.

Conclusion

Regseg is a variational framework for the simultaneous segmentation and registration of 3D dMRI data obtained from the human brain, where within-subject anatomical information is used as a reference. The registration method segments the target multivariate image into several competing regions, which are defined explicitly by their limiting surfaces. The surfaces are active and they evolve on a free-form deformation field supported by the B-spline basis. A descent optimization strategy is guided by shape gradients computed on the current partition of the target image. *Regseg* uses active contours without edges and it searches for homogeneous regions within the image. We tested *regseg* using digital phantoms by simulating T1w and T2w magnetic resonance imaging (MRI) warped with smooth random deformations. The resulting misregistration of the contours was significantly lower than the image resolution of the phantoms.

We proposed *regseg* for simultaneously segmenting and registering dMRI data to their corresponding T1w image from the same subject. We demonstrated the accuracy of the proposed method based on visual assessments of the results obtained by *regseg* and cross-comparisons with a widely used technique. Moreover, *regseg* does not require any images in addition to the minimal acquisition protocol, which only utilizes T1w and dMRI. As well as the proposed application to dMRI data, other potential uses of *regseg* are atlas-based segmentation and tracking objects in time-series.

Availability and reproducibility statement

We considered the reproducibility of our results as a design requirement. Therefore, we used real data obtained from a publicly available repository (the Human Connectome Project (Van Essen et al., 2012)) and all of the software utilized in this study is also publicly available. *Regseg* was implemented on top of ITK-4.6 (Insight Registration and Segmentation Toolkit, `http://www.itk.org`). The evaluation instruments (Figure 3) were implemented using *nipype* (Gorgolewski et al., 2011) to assess their reproducibility. All of the research elements (data, source code, figures, manuscript sources, etc.) involved in this study are publicly available under a unique package (Esteban and Zosso, 2015).

Author contributions

All the authors contributed to this study. OE implemented the method, designed and conducted the experiments, wrote the paper, simulated the phantoms, and prepared the real data. DZ devised and drafted the registration method, generated early phantom datasets, and collaborated in the implementation of the method. AD, MBC, and MJLC interpreted the results. AD, MBC, MJLC, JPT, and AS advised on all aspects of the study.

Acknowledgments

The authors thank Y. Alemán and G. Wollny for their thorough reviews of the manuscript, V. Estellers for early discussions at the beginning of this project, and L. A. Vese for her support during OE's research visits to her laboratory. We also thank A. Leemans for kindly sharing a p-code version of *ExploreDTI* from which the settings for *elastix* could be extracted.

DZ was supported by the Swiss National Science Foundation under grants PBELP2-137727, P300P2-147778, and NSF-DMS 1418812. This study was supported by the Spanish Ministry of Science and Innovation (projects TEC-2013-48251-C2-2-R and INNPACTO XIORT), Comunidad de Madrid (TOPUS) and European Regional Development Funds, the Center for Biomedical Imaging (CIBM) of the Geneva and Lausanne Universities and the EPFL, as well as the Leenaards and Louis Jeantet Foundations.

Appendix

Appendix 1. Simplifying the regularization term

The exponentials of the Thikonov regularization prior (6) have the general form $\mathbf{v}^T\mathbf{M}\mathbf{v}$. If $\mathbf{M}$ is a $n \times n$ diagonal matrix such that $\mathbf{M} = \mathbf{m}\,\mathbf{I}_n$, then:

$$\mathbf{v}^T\mathbf{M}\mathbf{v} = \mathbf{m} \cdot (\mathbf{v}^T\mathbf{I}_n\mathbf{v}) = \mathbf{m} \cdot \mathbf{v}^{\circ 2},$$

where we have introduced the Hadamard power notation[3].

In general, the anisotropy is aligned with the imaging axes, so $\mathbf{A}$ and $\mathbf{B}$ of (7) can be simplified to diagonal matrices, such that $\mathbf{A} = \boldsymbol{\alpha}\,\mathbf{I}_n$ and $\mathbf{B} = \boldsymbol{\beta}\,\mathbf{I}_n$. By substituting into equation (7), we obtain:

$$E(\mathbf{u}) = \text{Const.} + \sum_l \int_{\Omega_l} \mathcal{D}_l^2(\mathbf{f}')\, d\mathbf{r} + \int_\Omega \frac{1}{2}\left[\boldsymbol{\alpha} \cdot \mathbf{u}^{\circ 2} + \boldsymbol{\beta} \cdot (\nabla \mathbf{u})^{\circ 2}\right]\, d\mathbf{r}. \tag{A.1}$$

[3]The Hadamard power of a matrix or a vector is the power of its elements $\mathbf{M}^{\circ p} = ({m_{ij}}^p)$

References

P. Basser and C. Pierpaoli. Microstructural and physiological features of tissues elucidated by quantitative-diffusion-tensor MRI. *J Magn Reson*, 111(3):209–219, 1996. doi:10.1016/j.jmr.2011.09.022.

C. M. Bishop. *Pattern recognition and machine learning*, vol. 4. Springer SBM, LLC, 2006.

E. Caruyer, A. Daducci, M. Descoteaux, J.-C. Houde, J.-P. Thiran, and R. Verma. Phantomas: a flexible software library to simulate diffusion MR phantoms. In *23th ISMRM*, p. 6407, Milano, Italy, 2014.

T. F. Chan and L. A. Vese. Active contours without edges. *IEEE Trans Image Process*, 10(2):266–277, 2001. doi:10.1109/83.902291.

F. Commandeur, J. Velut, and O. Acosta. A VTK algorithm for the computation of the Hausdorff distance. *VTK Journal*, 839, 2011.

R. C. Craddock, S. Jbabdi, C.-G. Yan, J. T. Vogelstein, F. X. Castellanos, A. Di Martino, C. Kelly, K. Heberlein, S. Colcombe, and M. P. Milham. Imaging human connectomes at the macroscale. *Nat Meth*, 10(6):524–539, 2013. doi:10.1038/nmeth.2482.

M. Cuadra, L. Cammoun, T. Butz, O. Cuisenaire, and J. P. Thiran. Comparison and validation of tissue modelization and statistical classification methods in T1 weighted MR brain images. *IEEE Trans Med Imag*, 24(12):1548–1565, 2005. doi:10.1109/TMI.2005.857652.

M. Droske, W. Ring, and M. Rumpf. Mumford-Shah based registration: a comparison of a level set and a phase field approach. *Comput Vis Sci*, 12(3):101–114, 2009. doi:10.1007/s00791-008-0084-2.

D. B. Ennis and G. Kindlmann. Orthogonal tensor invariants and the analysis of diffusion tensor magnetic resonance images. *Magn Reson Med*, 55(1):136–146, 2006. doi:10.1002/mrm.20741.

O. Esteban and D. Zosso. RegSeg: Structure-informed segmentation and registration of brain MR images. *Zenodo [Software]*, 2015. doi:10.5281/zenodo.17345.

O. Esteban, A. Daducci, E. Caruyer, K. O'Brien, M.-J. Ledesma-Carbayo, M. Bach-Cuadra, and A. Santos. Simulation-based evaluation of susceptibility distortion correction methods in diffusion MRI for connectivity analysis. In *11th ISBI*, pp. 738–741, Beijing, China, 2014. doi:10.1109/ISBI.2014.6867976.

B. Fischl. Freesurfer. *NeuroImage*, 62(2):774–781, 2012. doi:10.1016/j.neuroimage.2012.01.021.

T. Gass, G. Székely, and O. Goksel. Simultaneous segmentation and multiresolution nonrigid atlas registration. *IEEE Trans Image Process*, 23(7):2931–2943, 2014. doi:10.1109/TIP.2014.2322447.

M. F. Glasser, S. N. Sotiropoulos, J. A. Wilson, T. S. Coalson, B. Fischl, J. L. Andersson, J. Xu, S. Jbabdi, M. Webster, J. R. Polimeni, D. C. Van Essen, and M. Jenkinson. The minimal preprocessing pipelines for the Human Connectome Project. *NeuroImage*, 80:105–124, 2013. doi:10.1016/j.neuroimage.2013.04.127.

K. Gorgolewski, C. D. Burns, C. Madison, D. Clark, Y. O. Halchenko, M. L. Waskom, and S. Ghosh. Nipype: a flexible, lightweight and extensible neuroimaging data processing framework in python. *Front Neuroinform*, 5:13, 2011. doi:10.3389/fninf.2011.00013.

S. Gorthi, V. Duay, X. Bresson, M. Bach Cuadra, F. J. Sánchez Castro, C. Pollo, A. S. Allal, and J.-P. Thiran. Active deformation fields: dense deformation field estimation for atlas-based segmentation using the active contour framework. *Med Image Anal*, 15(6): 787–800, 2011. doi:10.1016/j.media.2011.05.008.

D. N. Greve and B. Fischl. Accurate and robust brain image alignment using boundary-based registration. *NeuroImage*, 48(1):63–72, 2009. doi:10.1016/j.neuroimage.2009.06.060.

A. Hadjiprocopis, W. Rashid, and P. S. Tofts. Unbiased segmentation of diffusion-weighted magnetic resonance images of the brain using iterative clustering. *Magn Res Imag*, 23(8):877–885, 2005. doi:10.1016/j.mri.2005.07.010.

D. Han, V. Singh, J. Lee, E. Zakszewski, N. Adluru, T. Oakes, and A. Alexander. An experimental evaluation of diffusion tensor image segmentation using graph-cuts. In *EMBC*, vol. 31, pp. 5653–5656, Minneapolis, Minnesota, USA, 2009. doi:10.1109/IEMBS.2009.5333767.

A. Herbulot, S. Jehan-Besson, S. Duffner, M. Barlaud, and G. Aubert. Segmentation of vectorial image features using shape gradients and information measures. *J Math Imaging Vis*, 25(3):365–386, 2006. doi:10.1007/s10851-006-6898-y.

M. O. Irfanoglu, L. Walker, S. Sammet, C. Pierpaoli, and R. Machiraju. Susceptibility distortion correction for echo planar images with non-uniform B-Spline grid sampling: A diffusion tensor image study. In *14th MICCAI*, vol. 6892 of *LNCS*, pp. 174–181, Toronto, Canada, 2011. Springer Berlin Heidelberg. doi:10.1007/978-3-642-23629-7_22.

M. O. Irfanoglu, L. Walker, J. Sarlls, S. Marenco, and C. Pierpaoli. Effects of image distortions originating from susceptibility variations and concomitant fields on diffusion MRI tractography results. *NeuroImage*, 61(1):275–288, 2012. doi:10.1016/j.neuroimage.2012.02.054.

S. Jehan-Besson, M. Barlaud, and G. Aubert. DREAM2S: Deformable regions driven by an eulerian accurate minimization method for image and video segmentation. *Int J Comput Vis*, 53(1):45–70, 2003. doi:10.1023/A:1023031708305.

P. Jezzard and R. S. Balaban. Correction for geometric distortion in echo planar images from B0 field variations. *Magn Reson Med*, 34 (1):65–73, 1995. doi:10.1002/mrm.1910340111.

L. Jonasson. *Segmentation of diffusion weighted MRI using the level set framework*. Ph.D. Thesis, École Polytechnique Fédérale de Lausanne, Lausanne (Swizerland), 2005. doi:10.5075/epfl-thesis-3315.

S. Klein, M. Staring, K. Murphy, M. Viergever, and J. P. W. Pluim. elastix: A toolbox for intensity-based medical image registration. *IEEE Trans Med Imag*, 29(1):196–205, 2010. doi:10.1109/TMI.2009.2035616.

S. Kumazawa, T. Yoshiura, H. Honda, and F. Toyofuku. Improvement of partial volume segmentation for brain tissue on diffusion tensor images using multiple-tensor estimation. *J Digit Imaging*, pp. 1–10, 2013. doi:10.1007/s10278-013-9601-z.

J. Kybic, P. Thevenaz, A. Nirkko, and M. Unser. Unwarping of unidirectionally distorted EPI images. *IEEE Trans Med Imag*, 19(2):80–93, 2000. doi:10.1109/42.836368.

C. Le Guyader and L. A. Vese. A combined segmentation and registration framework with a nonlinear elasticity smoother. *Comput Vis Image Und*, 115(12):1689–1709, 2011. doi:10.1016/j.cviu.2011.05.009.

A. Leemans, B. Jeurissen, J. Sijbers, and D. Jones. ExploreDTI: a graphical toolbox for processing, analyzing, and visualizing diffusion MR data. In *17th ISMRM*, p. 3537, Hawaii, USA, 2009.

T. Liu, H. Li, K. Wong, A. Tarokh, L. Guo, and S. T. Wong. Brain tissue segmentation based on DTI data. *NeuroImage*, 38(1):114–123, 2007. doi:10.1016/j.neuroimage.2007.07.002.

C.-F. Lu, P.-S. Wang, Y.-C. Chou, H.-C. Li, B.-W. Soong, and Y.-T. Wu. Segmentation of diffusion-weighted brain images using expectation maximization algorithm initialized by hierarchical clustering. In *30th IEMBS*, vol. 30, pp. 5502–5505, Vancouver, Canada, 2008. doi:10.1109/IEMBS.2008.4650460.

D. Mumford and J. Shah. Optimal approximations by piecewise smooth functions and associated variational problems. *Comm Pure Appl Math*, 42(5):577–685, 1989. doi:10.1002/cpa.3160420503.

H.-H. Nagel and W. Enkelmann. An investigation of smoothness constraints for the estimation of displacement vector fields from image sequences. *IEEE Trans Pattern Anal Mach Intell*, 8(5):565–593, 1986. doi:10.1109/TPAMI.1986.4767833.

N. Paragios. A level set approach for shape-driven segmentation and tracking of the left ventricle. *IEEE Trans Med Imag*, 22(6):773–776, 2003. doi:10.1109/TMI.2003.814785.

K. M. Pohl, J. Fisher, W. E. L. Grimson, R. Kikinis, and W. M. Wells. A Bayesian model for joint segmentation and registration. *NeuroImage*, 31(1):228–39, 2006. doi:10.1016/j.neuroimage.2005.11.044.

M. Rousson, C. Lenglet, and R. Deriche. Level set and region based surface propagation for diffusion tensor MRI segmentation. In *ECCV*, vol. 3117, pp. 123–134, Berlin, Heidelberg, 2004. Springer Berlin Heidelberg. doi:10.1007/978-3-540-27816-0_11.

D. Rueckert, P. Aljabar, R. A. Heckemann, J. V. Hajnal, and A. Hammers. Diffeomorphic registration using B-Splines. In *9th MICCAI*, vol. 4191 of *LNCS*, pp. 702–709, Copenhagen, Denmark, 2006. Springer Berlin Heidelberg. doi:10.1007/11866763_86.

Z. S. Saad, D. R. Glen, G. Chen, M. S. Beauchamp, R. Desai, and R. W. Cox. A new method for improving functional-to-structural MRI alignment using local Pearson correlation. *NeuroImage*, 44(3):839–848, 2009. doi:10.1016/j.neuroimage.2008.09.037.

S. M. Smith, M. Jenkinson, H. Johansen-Berg, D. Rueckert, T. E. Nichols, C. E. Mackay, K. E. Watkins, O. Ciccarelli, M. Z. Cader, P. M. Matthews, and T. E. J. Behrens. Tract-based spatial statistics: Voxelwise analysis of multi-subject diffusion data. *NeuroImage*, 31(4): 1487–1505, 2006. doi:10.1016/j.neuroimage.2006.02.024.

C. Studholme, R. Constable, and J. Duncan. Accurate alignment of functional EPI data to anatomical MRI using a physics-based distortion model. *IEEE Trans Med Imag*, 19(11):1115–1127, 2000. doi:10.1109/42.896788.

R. Tao, P. T. Fletcher, S. Gerber, and R. T. Whitaker. A variational image-based approach to the correction of susceptibility artifacts in the alignment of diffusion weighted and structural MRI. In *IPMI*, vol. 5636 of *LNCS*, pp. 664–675, Williamsburg, VA, USA, 2009. Springer Berlin Heidelberg. doi:10.1007/978-3-642-02498-6_55.

T. Taoka, M. Morikawa, T. Akashi, T. Miyasaka, H. Nakagawa, K. Kiuchi, T. Kishimoto, and K. Kichikawa. Fractional anisotropy–threshold dependence in tract-based diffusion tensor analysis: evaluation of the uncinate fasciculus in Alzheimer disease. *AJNR Am J Neuroradiol*, 30(9):1700–1703, 2009. doi:10.3174/ajnr.A1698.

J.-D. Tournier, F. Calamante, and A. Connelly. MRtrix: Diffusion tractography in crossing fiber regions. *Int J Imag Syst Tech*, 22(1): 53–66, 2012. doi:10.1002/ima.22005.

N. J. Tustison, H. J. Johnson, T. Rohlfing, A. Klein, S. S. Ghosh, L. Ibanez, and B. B. Avants. Instrumentation bias in the use and evaluation of scientific software: recommendations for reproducible practices in the computational sciences. *Front Neurosci*, 7:162, 2013. doi:10.3389/fnins.2013.00162.

G. Unal and G. Slabaugh. Coupled PDEs for non-rigid registration and segmentation. In *CVPR*, vol. 1, pp. 168–175, San Diego, CA, USA, 2005. doi:10.1109/CVPR.2005.115.

D. Van Essen, K. Ugurbil, E. Auerbach, D. Barch, T. Behrens, R. Bucholz, A. Chang, L. Chen, M. Corbetta, S. Curtiss, S. Della Penna, D. Feinberg, M. Glasser, N. Harel, A. Heath, L. Larson-Prior, D. Marcus, G. Michalareas, S. Moeller, R. Oostenveld, S. Petersen, F. Prior, B. Schlaggar, S. Smith, A. Snyder, J. Xu, and E. Yacoub. The Human Connectome Project: A data acquisition perspective. *NeuroImage*, 62(4):2222–2231, 2012. doi:10.1016/j.neuroimage.2012.02.018.

K. Van Leemput, F. Maes, D. Vandermeulen, and P. Suetens. Automated model-based tissue classification of MR images of the brain. *IEEE Trans Med Imag*, 18(10):897–908, 1999. doi:10.1109/42.811270.

F. Wang, B. C. Vemuri, and S. J. Eisenschenk. Joint registration and segmentation of neuroanatomic structures from brain MRI. *Acad Radiol*, 13(9):1104–11, 2006. doi:10.1016/j.acra.2006.05.017.

M. Wu, L.-C. Chang, L. Walker, H. Lemaitre, A. S. Barnett, S. Marenco, and C. Pierpaoli. Comparison of EPI distortion correction methods in diffusion tensor MRI using a novel framework. In *11th MICCAI*, vol. 5242 of *LNCS*, pp. 321–329, New York, NY, USA, 2008. Springer Berlin Heidelberg. doi:10.1007/978-3-540-85990-1_39.

P. P. Wyatt and J. Noble. MAP MRF joint segmentation and registration of medical images. *Med Image Anal*, 7(4):539–552, 2003. doi:10.1016/S1361-8415(03)00067-7.

A. Yezzi, L. Zöllei, and T. Kapur. A variational framework for integrating segmentation and registration through active contours. *Med Image Anal*, 7(2):171–185, 2003. doi:10.1016/S1361-8415(03)00004-5.

L. Zhukov, K. Museth, D. Breen, R. Whitaker, and A. Barr. Level set modeling and segmentation of dt-MRI brain data. *J Electron Imaging*, 12(1):125–133, 2003. doi:10.1117/1.1527628.